

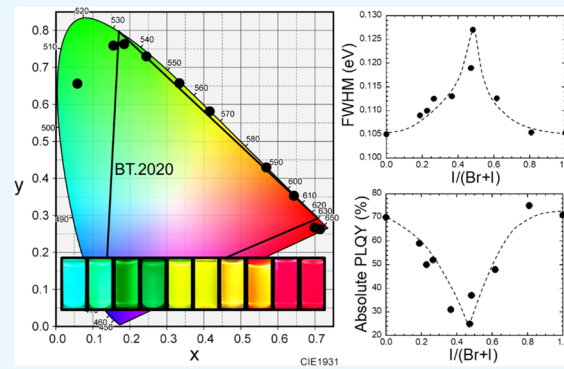
Green Photoluminescence of Perovskite $\text{CsPb}(\text{Br}_{1-x}\text{I}_x)_3$ Nanocrystals for Wide Color Gamut Displays

Simpei Miyata, Yoshiaki Iso,*^{ID} and Tetsuhiko Isobe*^{ID}

Department of Applied Chemistry, Faculty of Science and Technology, Keio University, 3-14-1 Hiyoshi, Kohoku-ku, Yokohama 223-8522, Japan

S Supporting Information

ABSTRACT: All-inorganic mixed-halide $\text{CsPb}(\text{Br}_{1-x}\text{I}_x)_3$ perovskite nanocrystals (NCs) are excellent candidates for green-emitting phosphors in wide color gamut displays; however, a detailed investigation of their photoluminescence (PL) properties based on the halide composition has been missing. In this work, we report a fundamental investigation of the changes in the PL properties of $\text{CsPb}(\text{Br}_{1-x}\text{I}_x)_3$ NCs. The PL color of the NCs, which were prepared by a hot-injection method, changed from green to red with increasing iodide composition (x). Almost ideal green emission close to the chromaticity coordinates of the green vertex of the BT.2020 standard was achieved by appropriately substituting iodide ions for bromide ions in monohalide CsPbBr_3 NCs. However, the PL peak width of the mix-halide NCs at $x \sim 0.5$ was 0.127 eV, which was broader than the 0.105 eV peak width of the monohalide CsPbBr_3 NCs. This phenomenon should be due to the compositional inhomogeneity among the individual $\text{CsPb}(\text{Br}_{1-x}\text{I}_x)_3$ NCs. On the other hand, the PL quantum yield (PLQY) for the monohalide CsPbBr_3 NCs decreased from 70 to 25% as x increased to 0.5. This result may be attributed to lattice distortion by the difference in the ionic radii of bromide and iodide. Improvements in the compositional inhomogeneity and lattice distortion would enhance the color purity of the green emission and the PLQY, respectively, of the $\text{CsPb}(\text{Br}_{1-x}\text{I}_x)_3$ NCs.



1. INTRODUCTION

Displays using patterned red-green-blue emitters without color filters can realize excellent color purity and a wider color reproduction range with higher emission efficiencies compared to those exploiting a white backlight passed through color filters.^{1,2} In the former method, a blue light-emitting diode (LED) is used as a blue light source, and green- and red-emitting phosphors are excited by the blue light to obtain green and red colors, respectively. BT.2020, which is a next-generation color standard for 4/8 K broadcasting, has a significantly larger range in the green than the conventional color system BT.709.^{3,4} To satisfy the BT.2020 standard, green-emitting phosphors with extremely high color purities are required for the green emitters in displays. Traditional lanthanide-doped green phosphors show photoluminescence (PL) from Tb^{3+} through 4f–4f transitions⁵ and from Eu^{2+} and Ce^{3+} through 4f–5d transitions;^{6,7} however, these phosphors cannot realize the required color purity because of their unnecessary PL peaks outside of the green region and broad PL peak widths. CdSe quantum dots (QDs) are the most commonly used nanophosphors that exhibit visible emission, including green emission,⁸ although Cd is highly toxic; therefore, other visible-emitting QDs such as CuInS_2 and InP have been identified as Cd-free alternative materials.^{9–11} Green-emitting InP QDs are one of the candidates for application in wide color gamut displays; however, the full

width at half-maximum (FWHM) of their green PL peak is ~50 nm, which is too broad to satisfy the green range of the BT.2020 standard.¹¹

In recent years, all-inorganic perovskite semiconductor nanocrystals (NCs) of the form CsPbX_3 ($X = \text{Cl}, \text{Br}, \text{I}$) have shown great development, triggered by a report from Protesescu et al.¹² The PL wavelength of these NCs can be tuned in the visible region between 410 and 700 nm by changing the halide composition, and smaller FWHMs of the PL peak with excellent PL quantum yields (PLQYs) of 50–90% have been observed.¹³ Moreover, to obtain these high PLQYs, core/shell structures, such as CdSe/ZnS QDs¹⁴ and InP/ZnS QDs,¹⁵ were not needed. The outstanding PL properties of CsPbX_3 NCs have attracted much attention;¹⁶ therefore, numerous studies on their synthetic methods,^{17–19} improvements in their stabilities,^{20–23} and optoelectronic applications, such as in LEDs and photodetectors,^{24,25} have been reported.

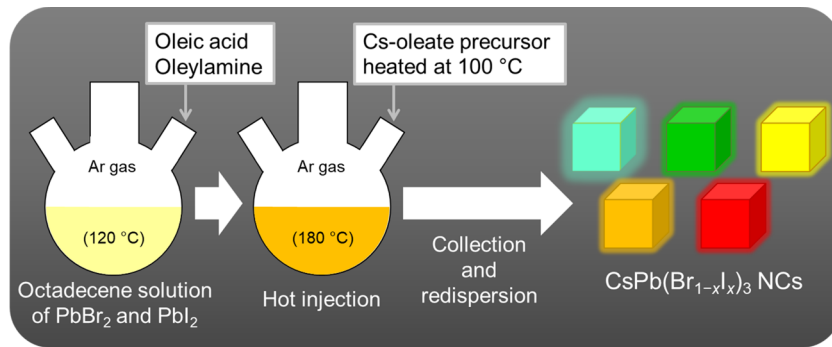
Green-emitting CsPbBr_3 NCs have a great potential to realize green emission for wide color gamut displays that satisfy the BT.2020 standard because of their highly pure PL color derived from a FWHM of ~20 nm. However, optimization of

Received: June 21, 2019

Accepted: August 22, 2019

Published: September 5, 2019



Scheme 1. Preparation of the $\text{CsPb}(\text{Br}_{1-x}\text{I}_x)_3$ NCs

the PL wavelength by controlling their band gap through partially substituting I^- for Br^- is required, whereas the PL peak width broadens as the iodide composition increases. The optical properties of perovskite CsPbBr_3 NCs have been studied by many groups, while a detailed characterization of mixed-halide perovskite NCs of the forms $\text{CsPb}(\text{Cl}_{1-x}\text{Br}_x)_3$ and $\text{CsPb}(\text{Br}_{1-x}\text{I}_x)_3$ is insufficient yet. Notably, perovskite $\text{CsPb}(\text{Cl}_{1-x}\text{I}_x)_3$ is hard to form at temperatures lower than 625 K.²⁶ We found works including characterization of the optical properties of perovskite NCs of the forms $\text{CsPb}(\text{Cl}_{1-x}\text{Br}_x)_3$ and $\text{CsPb}(\text{Br}_{1-x}\text{I}_x)_3$,^{12,27–29} however, a detailed discussion on the relationship between their comprehensive PL properties and the halide composition is missing. To realize next-generation displays using $\text{CsPb}(\text{Br}_{1-x}\text{I}_x)_3$, investigations of the changes in the PL peak width and PLQY as well as PL peak position are needed.

This work reports the halide composition-dependent PL properties of green-emitting $\text{CsPb}(\text{Br}_{1-x}\text{I}_x)_3$ NCs focused on the promising application of these materials in wide color gamut displays. We prepared the $\text{CsPb}(\text{Br}_{1-x}\text{I}_x)_3$ NCs by a hot-injection method (Scheme 1), which is the most frequently performed synthetic method,^{12,30} and characterized their elemental composition, crystal structure, morphology, and optical properties to discuss the influence of the halide composition on the PL properties, such as the peak position, FWHM, and PLQY.

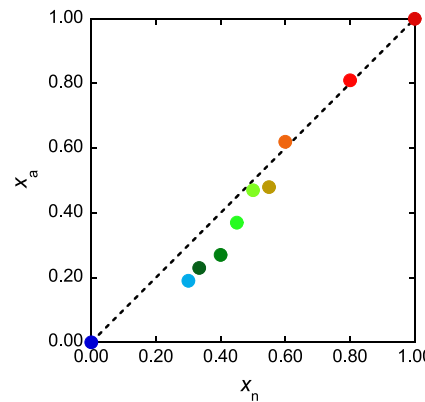
2. RESULTS AND DISCUSSION

2.1. Structures and Morphologies of Synthesized $\text{CsPb}(\text{Br}_{1-x}\text{I}_x)_3$ NCs. Elemental compositions of the $\text{CsPb}(\text{Br}_{1-x}\text{I}_x)_3$ powder samples were determined by an X-ray fluorescence (XRF) instrument, as shown in Table 1. Herein, the nominal and actual molar ratios of $\text{I}/(\text{Br} + \text{I})$ were defined

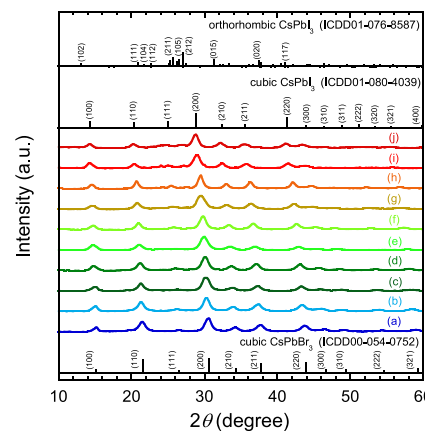
Table 1. Elemental Analysis of the Powder Samples of the $\text{CsPb}(\text{Br}_{1-x}\text{I}_x)_3$ NCs

x_n	Cs	Pb	Br	I	$\text{Br} + \text{I}$	x_a
0	0.7	1.1	3.3	0.0	3.3	0.00
0.30	0.7	1.0	2.7	0.6	3.3	0.19
0.33	1.0	1.0	2.4	0.7	3.1	0.23
0.40	0.9	1.0	2.2	0.9	3.1	0.27
0.45	0.7	1.0	2.1	1.2	3.3	0.37
0.50	0.8	1.0	1.7	1.5	3.2	0.47
0.55	0.7	1.1	1.6	1.5	3.1	0.48
0.60	0.9	0.9	1.2	1.9	3.1	0.62
0.80	0.7	1.3	0.6	2.4	3.0	0.81
1.00	0.8	1.3	0.0	2.9	2.9	1.00

as x_n and x_a , respectively. The measured compositional ratio of $\text{Cs/Pb}/(\text{Br} + \text{I})$ was 1:1:3, which corresponded to the stoichiometric ratio of $\text{CsPb}(\text{Br}_{1-x}\text{I}_x)_3$ for each of the samples. The value of x_a increased monotonically with increasing x_n , as plotted in Figure 1. We found a tendency for x_a to be smaller than x_n , possibly due to the higher reactivity of Br^- than that of I^- (Table 1).

**Figure 1.** Relationship between the nominal and actual molar ratios of $\text{I}/(\text{Br} + \text{I})$, i.e., x_n and x_a , respectively, for the powder samples of the $\text{CsPb}(\text{Br}_{1-x}\text{I}_x)_3$ NCs.

The X-ray diffraction (XRD) patterns of the powder samples are shown in Figure 2. All peaks at $x_n < 0.8$ were assigned to

**Figure 2.** XRD profiles for the powder samples of the $\text{CsPb}(\text{Br}_{1-x}\text{I}_x)_3$ NCs with x_n = (a) 0, (b) 0.30, (c) 0.33, (d) 0.40, (e) 0.45, (f) 0.50, (g) 0.55, (h) 0.60, (i) 0.80, and (j) 1.00.

the cubic phase $\text{CsPb}(\text{Br}_{1-x}\text{I}_x)_3$. Some orthorhombic phase $\text{CsPb}(\text{Br}_{1-x}\text{I}_x)_3$ was also observed when $x_n = 0.80$ and 1.00 (see enlarged XRD profiles in Figure S1). The orthorhombic phase could be formed from the cubic phase during storage³¹ because cubic CsPbI_3 is unstable under ambient conditions.³² The most stable phase of CsPbI_3 is the orthorhombic phase, while its cubic phase is metastable at room temperature.³² The peaks of the cubic phase shifted toward lower angles with increasing iodine content. Lattice spacings were calculated from the XRD peak of the (200) crystal plane by using Bragg's law

$$\lambda = 2d_{200} \sin \theta \quad (1)$$

where λ is the X-ray wavelength, d_{200} is the (200) lattice spacing, and θ is the reflection angle. As shown in Figure 3, the

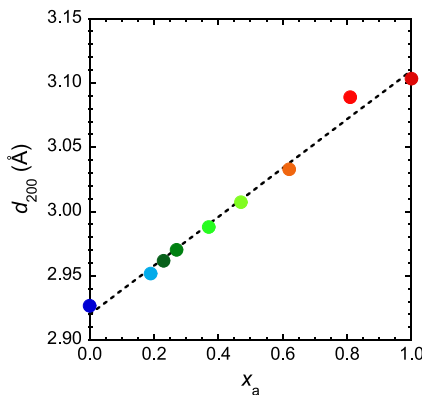


Figure 3. Change in lattice spacing (d_{200}) with changing x_a for the $\text{CsPb}(\text{Br}_{1-x}\text{I}_x)_3$ NCs.

lattice spacing linearly increased with increasing actual $\text{I}/(\text{Br} + \text{I})$, following Vegard's law. The ionic radii of Br^- and I^- in a 6-fold coordination site are 196 and 220 pm,³³ respectively; therefore, the increase in lattice spacing was caused by substituting I^- for Br^- .

Field-emission transmission electron microscopy (TEM) images of the samples are shown in Figure 4. The observed particles were rectangular regardless of their composition. The mean particle size was 9.7–12.0 nm (see the corresponding size distributions in Figure S2). The particle size increased as the $\text{I}/(\text{Br} + \text{I})$ ratio increased, as reported by previous studies.³⁴

Surface ligands of the $\text{CsPb}(\text{Br}_{1-x}\text{I}_x)_3$ NCs with $x_n = 0, 0.5$, and 1.0 were evaluated by Fourier transform infrared (FT-IR) spectroscopy (see Figure S3 and Table S1). There was no remarkable difference in their FT-IR spectra. Specific absorption peaks attributed to carboxylate and ammonium salts were observed, revealing surface modification by oleate and oleylammonium.

2.2. Optical Properties. Figure 5 displays toluene dispersions of the NCs under white light and 365 nm ultraviolet (UV) light. Their color under white light changed with changing iodide composition. The apparent color might be affected by the efficiency of their PL as well as their light absorption. The PL color under UV light changed from bluish-green to red with increasing iodide composition. Figure 6A shows the ultraviolet-visible (UV-vis) absorption spectra of the NC dispersions. The absorption edge red-shifted as the iodide composition increased. Figure S4 shows the Tauc plots

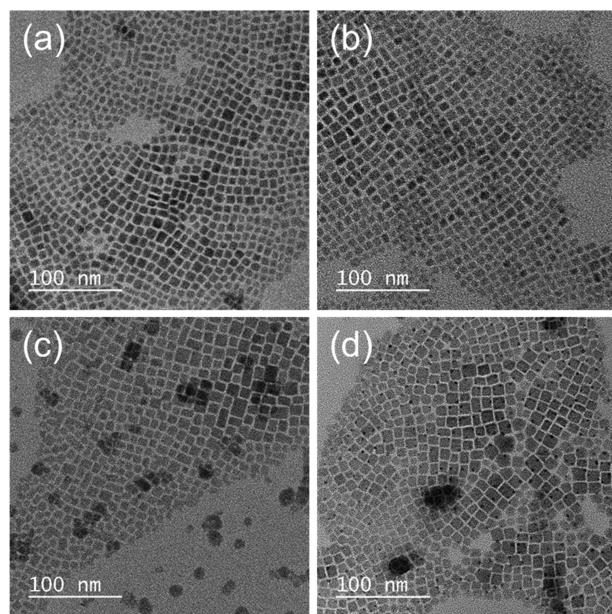


Figure 4. TEM images of the $\text{CsPb}(\text{Br}_{1-x}\text{I}_x)_3$ NCs with $x_n =$ (a) 0, (b) 0.30, (c) 0.50, and (d) 1.00.

calculated from the absorption spectra by the following equation

$$(\alpha h\nu)^{1/n} = k(h\nu - E_g) \quad (2)$$

where α is the absorbance, h is the Planck constant, ν is the frequency, k is a constant, and E_g is the band gap.³⁵ The value of n was 0.5 because cubic CsPbX_3 is a direct transition semiconductor. The determined band gap of the NCs linearly decreased with increasing x_a , as shown by line (a) in Figure 7. This is explained by the change in the band gap of the NCs as a result of the changing halide composition. According to the band structure of cubic CsPbX_3 , a change in the band gap is mainly caused by a shift of the valence band maximum, which is primarily composed of the p-orbitals of the halides.³⁶

The PL spectra of the NC dispersions are compared in Figure 6B. The NCs exhibit efficient PL emission through direct interband transitions.³⁷ The PL peak position is plotted as a function of x_a , as shown by line (b) in Figure 7. The PL peak energy decreased with increasing x_a due to the decrease in the band gap. The chromaticity coordinates converted from the PL spectra changed from (0.058, 0.656) to (0.680, 0.258) by tuning the contents of Br and I, as shown in Figure 8. The chromaticity coordinates (0.184, 0.763) at $x_n = 0.33$ was closest to the coordinates (0.170, 0.797) of the green vertex of the BT.2020 standard. To realize the ideal emission color at the green vertex, a narrower PL peak is required to improve the green color purity. As shown in Figure 9, the FWHM of the PL peak reached its maximum at $x_a = 0.48$, while it decreased as the halide composition became closer to containing only bromide or iodide. The increase in the FWHM could be explained by the widening of the particle size distribution and the compositional inhomogeneity of Br^- and I^- between the individual NCs. Swarnkar et al. synthesized CsPbBr_3 NCs that were 11 nm in size by the hot-injection method and found that there was no significant difference between the PL peak widths from their ensemble and single nanocrystals.³⁸ In this work, the NCs prepared by the hot-injection method included particles larger than 10 nm, from TEM observation (see Figure S2),

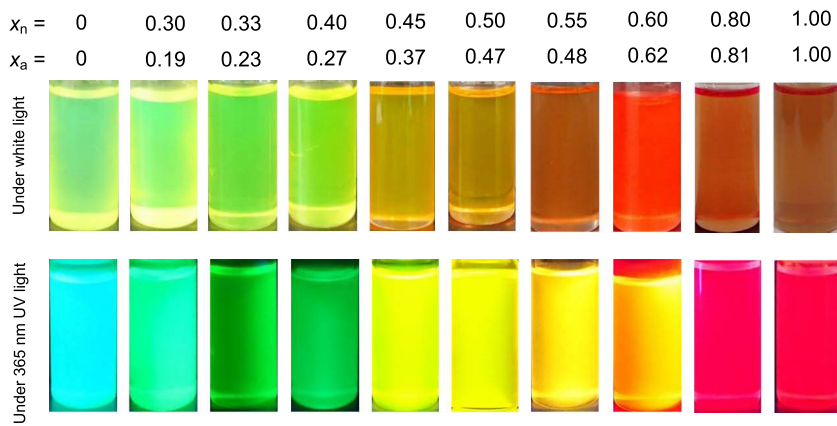


Figure 5. Photographs of the $\text{CsPb}(\text{Br}_{1-x}\text{I}_x)_3$ NC dispersions under white light and 365 nm UV light.

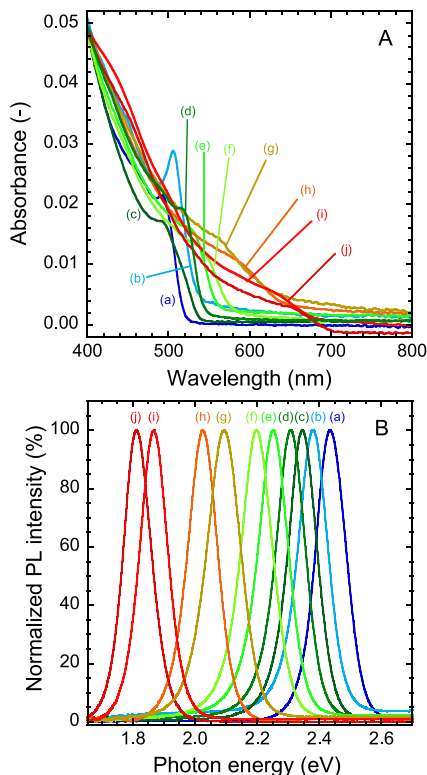


Figure 6. (A) UV-vis absorption spectra and (B) PL spectra ($\lambda_{\text{ex}} = 400 \text{ nm}$) of $\text{CsPb}(\text{Br}_{1-x}\text{I}_x)_3$ NC dispersions with $x_n =$ (a) 0, (b) 0.30, (c) 0.33, (d) 0.40, (e) 0.45, (f) 0.50, (g) 0.55, (h) 0.60, (i) 0.80, and (j) 1.00.

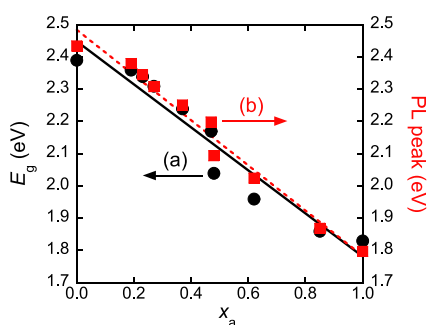


Figure 7. Changes in the (a) band gap (E_g) and (b) PL peak energy with changing x_a in $\text{CsPb}(\text{Br}_{1-x}\text{I}_x)_3$ NC dispersions.

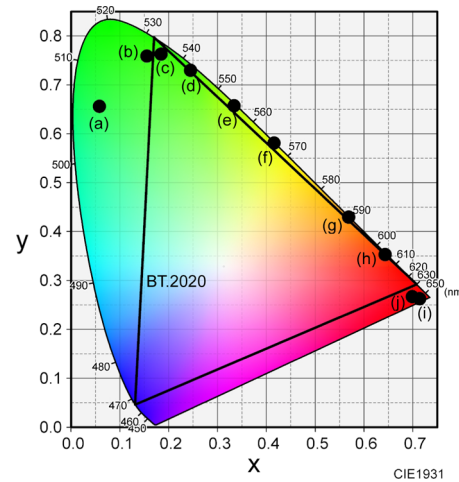


Figure 8. Chromaticity coordinates converted from the PL spectra of $\text{CsPb}(\text{Br}_{1-x}\text{I}_x)_3$ NC dispersions with $x_n =$ (a) 0, (b) 0.30, (c) 0.33, (d) 0.40, (e) 0.45, (f) 0.50, (g) 0.55, (h) 0.60, (i) 0.80, and (j) 1.00. $\lambda_{\text{ex}} = 400 \text{ nm}$.

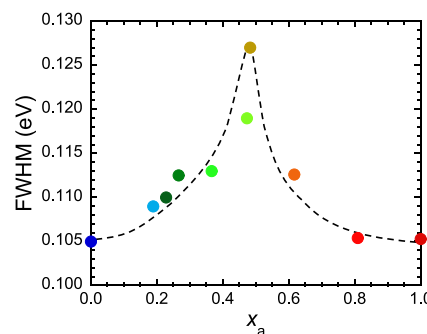


Figure 9. Changes in the FWHM of the PL peak with changing x_a in the $\text{CsPb}(\text{Br}_{1-x}\text{I}_x)_3$ NCs.

while the exciton Bohr diameters of CsPbBr_3 and CsPbI_3 are 7 and 12 nm,¹² respectively. In a typical hot-injection method for perovskite CsPbX_3 NCs, most of the formed NCs are >10 nm in size due to their rapid growth rate.³⁹ The quantum size effect in the prepared NCs should not be strong; therefore, the influence of the inhomogeneity of the particle sizes on the FWHM of the PL peak should be negligible. The FWHM decreased as the halide composition approached that of a monohalide bromide or iodide, whereas broadening of the PL

peak was observed as x_a approached 0.5. This might be due to compositional inhomogeneity between individual NCs. According to the elemental analysis of randomly selected single NCs by energy-dispersive X-ray spectroscopy (EDX), local I/(Br + I) compositions of 0.20 and 0.46 were detected for NCs prepared at $x_n = 0.50$ (see Figure S5 and Table S2). Thus, there was compositional inhomogeneity between individual NCs, causing an increase in the PL peak width. The increase in FWHM is possibly caused by the photo-induced phase segregation, which is known for mixed-halide lead perovskites.⁴⁰ However, obvious separation of the PL peak was not observed in Figure 6B.

As shown in Figure 10, the absolute PLQY of the NCs reached the minimum value at $x_a = 0.47$, while it increased as

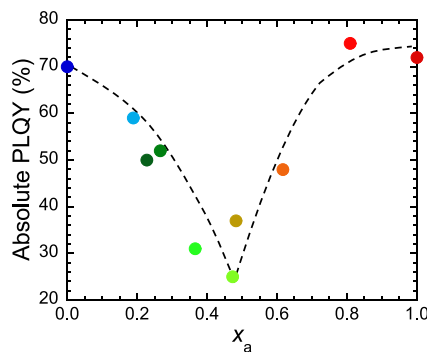


Figure 10. Changes in the absolute PLQY with changing x_a in the $\text{CsPb}(\text{Br}_{1-x}\text{I}_x)_3$ NCs.

x_a approached both 0 and 1. This result should be due to lattice distortion induced by the difference between the ionic radii of Br^- and I^- . The PLQY decreased with the formation of lattice defects that caused nonradiative recombination; therefore, relaxation of the distorted lattice would enhance the PLQY. Influence of defects on PLQY is generally discussed by PL decay curves. However, average PL lifetimes of the $\text{CsPb}(\text{Br}_{x-1}\text{I}_x)_3$ NCs calculated from the PL decay curves increased from 4.6 to 43.9 ns with increasing x_a (see Figure S6 and Table S3), as reported in previous works.⁴¹ Intrinsically, there is a large difference in PL lifetimes of CsPbBr_3 NCs and CsPbI_3 NCs. The behavior of PLQY in Figure 10 therefore could not be related to the PL lifetimes.

To improve the lattice distortion of ABX_3 crystals with a cubic perovskite structure, substitution of the A-site or B-site cations with other cations of different sizes is effective. According to the previous work by Hu et al.,⁴² perovskite $(\text{FA}_{0.83}\text{MA}_{0.17})\text{Pb}(\text{I}_{0.83}\text{Br}_{0.17})$ was stabilized through lattice shrinkage by substituting Cs^+ for the larger A-site cations; herein, FA and MA are formamidinium $\{\text{(NH}_2\text{)}_2\text{CH}^+\}$ and methylammonium $\{\text{CH}_3\text{NH}_3^+\}$ cations, respectively. The tolerance factor T , which is an indicator of the stability of an ABX_3 crystal with a cubic perovskite structure, can be represented by the following equation

$$T = \frac{R_A + R_X}{\sqrt{2}(R_B + R_X)} \quad (3)$$

where R_A , R_B , and R_X are radii of the A-, B-, and X-site ions, for which the coordination numbers are twelve, six, and six, respectively.⁴² For CsPbBr_3 and CsPbI_3 , their T values were calculated to be 0.862 and 0.851, respectively, based on their ionic radii, which are 188 pm for Cs^+ , 119 pm for Pb^{2+} , 196 pm

for Br^- , and 220 pm for I^- .³³ The cubic perovskite structure is most stable at $T = 1$; therefore, the lattice distortion of $\text{CsPb}(\text{Br}_{1-x}\text{I}_x)_3$ would improve with increasing T . This can be achieved by substituting a larger monovalent cation for Cs^+ or a smaller divalent cation for Pb^{2+} in $\text{CsPb}(\text{Br}_{1-x}\text{I}_x)_3$. CH_3NH_3^+ and $(\text{NH}_2)_2\text{CH}^+$, for which the ionic radii are 217 and 253 pm, respectively, are candidates for the larger monovalent cations.⁴³ However, organic-inorganic perovskite materials are more readily degraded than all-inorganic perovskite materials.⁴⁴ All-inorganic perovskite NCs are promising for long-term use, whereas substituting a larger inorganic monovalent cation for Cs^+ in the A-site is unfeasible. Substitution of Pb^{2+} in the B-site with smaller inorganic divalent cations is a good way to relax the lattice distortion and improve the PLQY.

3. CONCLUSIONS

We prepared $\text{CsPb}(\text{Br}_{1-x}\text{I}_x)_3$ perovskite NCs by a hot-injection method and investigated the relationship between the halide composition and their optical properties. The band gap and PL peak energy of the NCs decreased with increasing iodine content. The emission color changed from bluish-green to red. The chromaticity coordinates (0.184, 0.763) at $x_a = 0.23$ were closest to the coordinates (0.170, 0.797) of the green vertex of the BT.2020 standard. Thus, it is useful to substitute an appropriate amount of I^- for Br^- in CsPbBr_3 NCs for their application as the green emitter in wide color gamut displays. The FWHM of the mix-halide NCs at $x_a \sim 0.5$ was 0.127 eV, which was broader than the 0.105 eV FWHM of the monohalide CsPbBr_3 NCs. This result should be due to the compositional inhomogeneity among the individual NCs. On the other hand, the PLQY decreased from ~70% for the monohalide CsPbBr_3 NCs to 25% as x_a approached 0.5. This result may be attributed to the lattice distortion induced by the difference in the ionic radii of Br^- and I^- . Homogenization of the halide composition among the individual NCs and relaxation of the lattice distortion would improve the green color and PLQY of the $\text{CsPb}(\text{Br}_{1-x}\text{I}_x)_3$ NCs, respectively. The appropriate mixed-halide composition almost realized the ideal green emission satisfying the BT.2020 standard, but increase in the iodide ratio may decrease the stability of the $\text{CsPb}(\text{Br}_{1-x}\text{I}_x)_3$ NCs. Improvement on the stability would be required for practical applications.

4. EXPERIMENTAL SECTION

4.1. Materials. Cs_2CO_3 (99.99%, Mitsuwa Pure Chemical), PbBr_2 (99%, Mitsuwa Pure Chemical), and PbI_2 (99%, Sigma-Aldrich) were used as received without further purification. Additionally, 1-octadecene (ODE; >90.0%, Tokyo Chemical Industry), oleic acid (OA; >85.0%, Tokyo Chemical Industry), oleyleamine (OAm; 80–90%, Acros Organics), *tert*-butyl alcohol (>99.0% Tokyo Chemical Industry), methyl acetate (99.5%, Kanto Chemical), and toluene (99.5%, Kanto Chemical) were dehydrated over molecular sieves (3A 1/8, Wako Pure Chemical Industries) prior to use.

4.2. Preparation of Cs-Oleate Precursor. Cs_2CO_3 (1.25 mmol), ODE (20.0 mL), and OA (1.3 mL) were mixed and degassed for 1 h at 120 °C and then purged with Ar gas. A Cs-oleate precursor solution was obtained by heating the mixture to 150 °C. The resulting solution was preheated at 100 °C before being injected into the reaction flask.

4.3. Synthesis of CsPbX_3 ($X = \text{Br}$ and I) NCs. ODE (5.0 mL), 0.376 ($1 - x_n$) mmol PbBr_2 , and 0.376 x_n mmol PbI_2 (x_n

$= 0, 0.30, 0.33, 0.40, 0.45, 0.50, 0.55, 0.60, 0.80,$ and 1.00) were loaded into a 4-neck flask and degassed for 1 h at 120°C and then purged with Ar gas. OA (1.0 mL) and OAm (1.0 mL) were injected into the flask, and after completely dissolving the salt mixture, the temperature was raised to 180°C . The Cs-oleate precursor solution (0.8 mL) was swiftly injected into the reaction flask and then cooled in an ice water bath after 5 s. Crystallized nanoparticles were precipitated by adding *tert*-butyl alcohol (25.0 mL). Alternatively, methyl acetate (25.0 mL) was used when $x = 1.00$. The NCs were collected by centrifugation at $\sim 11\,000\text{g}$ (10 000 rpm using a rotor with a diameter of 10 cm) for 5 min and then redispersed in toluene. Subsequently, the NC powder was prepared by drying the collected NCs under vacuum overnight.

4.4. Characterization. The elemental ratios of the NC powders were measured using an XRF analyzer (ZSXmini II, Rigaku). Powder XRD profiles were obtained using an X-ray diffractometer (Rint-2200, Rigaku) with a Cu $K\alpha$ radiation source and monochromator. The NC morphologies were observed by field-emission TEM (Tecnai G², FEI). The TEM samples were prepared by vacuum drying a drop of a NC dispersion on carbon-reinforced collodion-coated copper grids (COL-C10, Oken Shoji) overnight. The EDX was performed on the same apparatus. FT-IR absorption spectra of the samples in KBr disks were recorded on an FT-IR spectrometer (FT/IR-4200, JASCO). UV-vis absorption spectra of the NC dispersions were measured using an optical absorption spectrometer (V-570, JASCO). The PL spectra of the NC dispersions were measured using a fluorescence spectrometer (FP-6500, JASCO). Each spectral response was calibrated using an ethylene glycol solution of rhodamine B (5.5 g L^{-1}) and a standard light source (ESC-333, JASCO). Absolute PLQYs were measured using a quantum efficiency measurement system (QE-2000-311C, Otsuka Electronics). The PL decay curves were recorded on a fluorescence lifetime spectrometer (Quantaurus-Tau C11367, Hamamatsu Photonics). Herein, the PL decay curves were fitted with the following biexponential function

$$f(t) = A_1 \exp\left(-\frac{t}{\tau_1}\right) + A_2 \exp\left(-\frac{t}{\tau_2}\right) \quad (4)$$

where t is time, A_1 and A_2 are the amplitudes, and τ_1 and τ_2 are the PL decay times. The average PL lifetime $\langle\tau\rangle$ was calculated using eq 5.

$$\tau = \frac{A_1\tau_1^2 + A_2\tau_2^2}{A_1\tau_1 + A_2\tau_2} \quad (5)$$

■ ASSOCIATED CONTENT

S Supporting Information

The Supporting Information is available free of charge on the ACS Publications website at DOI: [10.1021/acsomega.9b01858](https://doi.org/10.1021/acsomega.9b01858).

Enlarged XRD profiles of the powder samples of the $\text{CsPb}(\text{Br}_{1-x}\text{I}_x)_3$ NCs (Figure S1); size distributions from the TEM images in Figure 4 (Figure S2); FT-IR spectra (Figure S3); peak assignment for the FT-IR spectra (Table S1); Tauc plots converted from the absorption spectra in Figure 6A (Figure S4); dark-field TEM images of the $\text{CsPb}(\text{Br}_{1-x}\text{I}_x)_3$ NCs at $x_n = 0.50$ (Figure S5); EDX results for individual NCs (Table S2); PL decay

curves (Figure S6); and results for the PL lifetime analysis (Table S3) ([PDF](#))

■ AUTHOR INFORMATION

Corresponding Authors

*E-mail: iso@appc.keio.ac.jp. Tel: +81 45 566 1558. Fax: +81 45 566 1551. (Y.I.).

*E-mail: isobe@appc.keio.ac.jp. Tel: +81 45 566 1554. Fax: +81 45 566 1551. (T.I.).

ORCID

Yoshiki Iso: [0000-0001-7483-2828](https://orcid.org/0000-0001-7483-2828)

Tetsuhiko Isobe: [0000-0002-0868-5425](https://orcid.org/0000-0002-0868-5425)

Notes

The authors declare no competing financial interest.

■ ACKNOWLEDGMENTS

The authors are grateful for the financial supports by the Futaba Research Grant Program of the Futaba Foundation (T.I.), the Iketani Science and Technology Foundation (T.I.), and the Shorai Foundation for Science and Technology (Y.I.).

■ REFERENCES

- Supran, G. J.; Shirasaki, Y.; Song, K. W.; Caruge, J. M.; Kazlas, P. T.; Sullivan, S. C.; Andrew, T. L.; Bawendi, M. G.; Bulovic, V. QLEDs for displays and solid-state lighting. *MRS Bull.* **2013**, *38*, 703–711.
- Anikeeva, P. O.; Halpert, J. E.; Bawendi, M. G.; Bulovic, V. Quantum dot light-emitting devices with electroluminescence tunable over the entire visible spectrum. *Nano Lett.* **2009**, *9*, 2532–2536.
- Sugawara, M.; Choi, S. Y.; Wood, D. Ultra-high-definition television (Rec. ITU-R BT.2020): a generational leap in the evolution of television. *IEEE Signal Process. Mag.* **2014**, *31*, 170–174.
- Zhu, R.; Luo, Z.; Chen, H.; Dong, Y.; Wu, S. T. Realizing Rec.2020 color gamut with quantum dot displays. *Opt. Express* **2015**, *23*, 23680–23693.
- Fu, Z.; Bu, W. High efficiency green-luminescent $\text{LaPO}_4:\text{Ce}, \text{Tb}$ hierarchical nanostructures: Synthesis, characterization, and luminescence properties. *Solid State Sci.* **2008**, *10*, 1062–1067.
- Xie, R. J.; Hirosaki, N.; Li, H. L.; Li, Y. Q.; Mitomo, M. Synthesis and photoluminescence properties of β -sialon: Eu^{2+} ($\text{Si}_{6-z}\text{Al}_z\text{O}_z\text{N}_{8-z}:\text{Eu}^{2+}$). *J. Electrochem. Soc.* **2007**, *154*, J314–J319.
- Shimomura, Y.; Honma, T.; Shigeiwa, M.; Akai, T.; Okamoto, K.; Kijima, N. Photoluminescence and crystal structure of green-emitting $\text{Ca}_2\text{Sc}_2\text{Si}_3\text{O}_{12}:\text{Ce}^{3+}$ phosphor for white light emitting diodes. *J. Electrochem. Soc.* **2007**, *154*, J35–J38.
- Pu, C.; Qin, H.; Gao, Y.; Zhou, J.; Wang, P.; Peng, X. Synthetic control of exciton behavior in colloidal quantum dots. *J. Am. Chem. Soc.* **2017**, *139*, 3302–3311.
- Wada, C.; Iso, Y.; Isobe, T.; Sasaki, H. Preparation and photoluminescence properties of yellow-emitting $\text{CuInS}_2/\text{ZnS}$ quantum dots embedded in TMAS-derived silica. *RSC Adv.* **2017**, *7*, 7936–7943.
- Watanabe, T.; Wada, C.; Iso, Y.; Isobe, T.; Sasaki, H. Preparation of photostable fluorescent InP/ZnS quantum dots embedded in TMAS-derived silica. *ECS J. Solid State Sci. Technol.* **2017**, *6*, R75–R80.
- Watanabe, T.; Iso, Y.; Isobe, T.; Sasaki, H. Photoluminescence color stability of green-emitting InP/ZnS core/shell quantum dots embedded in silica prepared via hydrophobic routes. *RSC Adv.* **2018**, *8*, 25526–25533.
- Protesescu, L.; Yakunin, S.; Bodnarchuk, M. I.; Krieg, F.; Caputo, R.; Hendon, C. H.; Yang, R. X.; Walsh, A.; Kovalenko, M. V. Nanocrystals of cesium lead halide perovskites (CsPbX_3 , X = Cl, Br, and I): Novel optoelectronic materials showing bright emission with wide color gamut. *Nano Lett.* **2015**, *15*, 3692–3696.

- (13) Kovalenko, M. V.; Protesescu, L.; Bodnarchuk, M. I. Properties and potential optoelectronic applications of lead halide perovskite nanocrystals. *Science* **2017**, *358*, 745–750.
- (14) Dabbousi, B. O.; Rodriguez-Viejo, J.; Mikulec, F. V.; Heine, J. R.; Mattoussi, H.; Ober, R.; Jensen, K. F.; Bawendi, M. G. (CdSe)ZnS core-shell quantum dots: Synthesis and characterization of a size series of highly luminescent nanocrystallites. *J. Phys. Chem. B* **1997**, *101*, 9463–9475.
- (15) Li, L.; Reiss, P. One-pot synthesis of highly luminescent InP/ZnS nanocrystals without precursor injection. *J. Am. Chem. Soc.* **2008**, *130*, 11588–11589.
- (16) Iso, Y.; Isobe, T. Review-synthesis, luminescent properties, and stabilities of cesium lead halide perovskite nanocrystals. *ECS J. Solid State Sci. Technol.* **2018**, *7*, R3040–R3045.
- (17) Tong, Y.; Bladt, E.; Ayyuler, M. F.; Manzi, A.; Milowska, K. Z.; Hintermayr, V. A.; Docampo, P.; Bals, S.; Urban, A. S.; Polavarapu, L.; Feldmann, J. Highly luminescent cesium lead halide perovskite nanocrystals with tunable composition and thickness by ultrasonication. *Angew. Chem., Int. Ed.* **2016**, *55*, 13887–13892.
- (18) Sun, S.; Yuan, D.; Xu, Y.; Wang, A.; Deng, Z. Ligand-mediated synthesis of shape-controlled cesium lead halide perovskite nanocrystals via reprecipitation process at room temperature. *ACS Nano* **2016**, *10*, 3648–3657.
- (19) Ye, S.; Yu, M.; Zhao, M.; Song, J.; Qu, J. Low temperature synthesis of high-quality all-inorganic cesium lead halide perovskite nanocrystals in open air and their upconversion luminescence. *J. Alloys Compd.* **2018**, *730*, 62–70.
- (20) Chen, J.; Liu, D.; Al-Marri, M. J.; Nuutila, L.; Lehtivuori, H.; Zheng, K. Photo-stability of CsPbBr₃ perovskite quantum dots for optoelectronic application. *Sci. China Mater.* **2016**, *59*, 719–727.
- (21) Li, Z.; Kong, L.; Huang, S.; Li, L. Highly luminescent and ultrastable CsPbBr₃ perovskite quantum dots incorporated into a silica/alumina monolith. *Angew. Chem., Int. Ed.* **2017**, *56*, 8134–8138.
- (22) Diroll, B. T.; Nedelcu, G.; Kovalenko, M. V.; Schaller, R. D. High-temperature photoluminescence of CsPbX₃ (X = Cl, Br, I) nanocrystals. *Adv. Funct. Mater.* **2017**, *27*, No. 1606750.
- (23) Kosugi, T.; Iso, Y.; Isobe, T. Effects of oleic acid on the stability of perovskite CsPbBr₃ quantum dot dispersions. *Chem. Lett.* **2019**, *48*, 349–352.
- (24) Song, J.; Li, J.; Li, X.; Xu, L.; Dong, Y.; Zeng, H. Quantum dot light emitting diodes based on inorganic perovskite cesium lead halides (CsPbX₃). *Adv. Mater.* **2015**, *27*, 7162–7167.
- (25) Ramasamy, P.; Lim, D. H.; Kim, B.; Lee, S. H.; Lee, M. S.; Lee, J. S. All-inorganic cesium lead halide perovskite nanocrystals for photodetector applications. *Chem. Commun.* **2016**, *52*, 2067–2070.
- (26) Yin, W. J.; Yan, Y.; Wei, S. H. Anomalous alloy properties in mixed halide perovskites. *J. Phys. Chem. Lett.* **2014**, *5*, 3625–3631.
- (27) Bi, C.; Wang, S.; Wen, W.; Yuan, J.; Cao, G.; Tian, J. Room-temperature construction of mixed-halide perovskite quantum dots with high photoluminescence quantum yield. *J. Phys. Chem. C* **2018**, *122*, 5151–5160.
- (28) Cottingham, P.; Brutchey, R. L. Compositionally dependent phase identity of colloidal CsPbBr_{3-x}I_x quantum dots. *Chem. Mater.* **2016**, *28*, 7574–7577.
- (29) Pradhan, B.; Mushtaq, A.; Roy, D.; Sain, S.; Das, B.; Ghorai, U. K.; Pal, S. K.; Acharya, S. Postsynthesis spontaneous coalescence of mixed-halide perovskite nanocubes into phase-stable single-crystalline uniform luminescent nanowires. *J. Phys. Chem. Lett.* **2019**, *10*, 1805–1812.
- (30) Zhang, D.; Eaton, S. W.; Yu, Y.; Dou, L.; Yang, P. Solution-phase synthesis of cesium lead halide perovskite nanowires. *J. Am. Chem. Soc.* **2015**, *137*, 9230–9233.
- (31) Wang, C.; Chesman, A. S. R.; Jasieniak, J. J. Stabilizing the cubic perovskite phase of CsPbI₃ nanocrystals by using an alkyl phosphinic acid. *Chem. Commun.* **2017**, *53*, 232–235.
- (32) Eperon, G. E.; Paterno, G. M.; Sutton, R. J.; Zampetti, A.; Haghaghirad, A. A.; Cacialli, F.; Snaith, H. J. Inorganic caesium lead iodide perovskite solar cells. *J. Mater. Chem. A* **2015**, *3*, 19688–19695.
- (33) Shannon, R. D. Revised effective ionic radii and systematic studies of interatomic distances in halides and chalcogenides. *Acta Cryst.* **1976**, *A32*, 751–767.
- (34) Makarov, N. S.; GSuo, S.; Isaenko, O.; Liu, W.; Robel, I.; Klimov, V. I. Spectral and dynamical properties of single excitons, biexcitons, and trions in cesium-lead-halide perovskite quantum dots. *Nano Lett.* **2016**, *16*, 2349–2362.
- (35) Tauc, J.; Menth, A. States in the gap. *J. Non-Cryst. Solids* **1972**, *8–10*, 569–585.
- (36) Ravi, V. K.; Marked, G. B.; Nag, A. Band edge energies and excitonic transition probabilities of colloidal CsPbX₃ (X = Cl, Br, I) perovskite nanocrystals. *ACS Energy Lett.* **2016**, *1*, 665–671.
- (37) Huang, H.; Polavarapu, L.; Sichert, J. A.; Susha, A. S.; Urban, A. S.; Rogach, A. L. Colloidal lead halide perovskite nanocrystals: Synthesis, optical properties and applications. *NPG Asia Mater.* **2016**, *8*, No. e328.
- (38) Swarnkar, A.; Chulliyil, R.; Ravi, V. K.; Irfanullah, M.; Chowdhury, A.; Nag, A. Colloidal CsPbBr₃ perovskite nanocrystals: Luminescence beyond traditional quantum dots. *Angew. Chem., Int. Ed.* **2015**, *54*, 15424–15428.
- (39) Dong, Y.; Qiao, T.; Kim, D.; Parobek, D.; Rossi, D.; Son, D. H. Precise control of quantum confinement in cesium lead halide perovskite quantum dots via thermodynamic equilibrium. *Nano Lett.* **2018**, *18*, 3716–3722.
- (40) Yoon, S. J.; Draguta, S.; Manser, J. S.; Sharia, O.; Schneider, W. F.; Kuno, M.; Kamat, P. V. Tracking iodide and bromide ion segregation in mixed halide lead perovskites during photoirradiation. *ACS Energy Lett.* **2016**, *1*, 290–296.
- (41) Makarov, N. S.; Guo, S.; Isaenko, O.; Liu, W.; Robel, I.; Klimov, V. I. Spectral and dynamical properties of single excitons, biexcitons, and trions in cesium–lead-halide perovskite quantum dots. *Nano Lett.* **2016**, *16*, 2349–2362.
- (42) Hu, Y.; Ayyuler, M. F.; Petrus, M. L.; Bein, T.; Docampo, P. Impact of rubidium and cesium cations on the moisture stability of multiple-cation mixed-halide perovskites. *ACS Energy Lett.* **2017**, *2*, 2212–2218.
- (43) Nagabushana, G. P.; Shivaramaiah, R.; Navrotsky, A. Direct calorimetric verification of thermodynamic instability of lead halide hybrid perovskites. *Proc. Natl. Acad. Sci. U.S.A.* **2016**, *113*, 7717–7721.
- (44) Carrero, S. G.; Galian, R. E.; Pietro, J. P. Organic-inorganic and all-inorganic lead halide nanoparticles. *J. Opt. Soc. Am.* **2016**, *24*, A285–A301.